




# A Microwave Sensing and Imaging Method for Multiphase Flow Metering of Crude Oil Pipes

Fatemeh Modares Sabzevari , *Student Member, IEEE*, Robert S. C. Winter , *Member, IEEE*, Daniel Oloumi , *Member, IEEE*, and Karumudi Rambabu, *Member, IEEE*

**Abstract**—This article proposes a microwave sensing and imaging method for multiphase flow monitoring and metering in oil and gas pipes. The ultrawideband (UWB) synthetic aperture radar (SAR) technique is used to create a high-resolution image of the pipe cross section. The image is, then, used to estimate each phase volume by extracting the edge of each phase. Additionally, the generalized impulsization technique is presented and applied to reconstruct a sharp-image, and decrease the error in flow rate estimation. Furthermore, a novel technique to enhance the detectability of weak targets in the images is proposed. Finally, a novel sectional image reconstruction technique is also applied to improve the imaging and metering of the stratified flows. All the proposed techniques are evaluated through experiments. This study demonstrates the ability to accurately estimate the crude oil flow rate with a maximum error of 3.8%. These results show that UWB SAR is capable of providing a reliable and noninvasive solution for multiphase flow metering.

**Index Terms**—Oil pipe monitoring, synthetic aperture radar (SAR), ultrawideband (UWB) technology.

## I. INTRODUCTION

**R**EAL-TIME, accurate, and nondestructive flow monitoring and measuring of multiphase flows are widely needed in many industries, such as food, aerospace, geothermal, and oil and gas industries [1]–[3]. For example, real-time multiphase flow metering (MFM) is recognized as one of the best methods for optimizing field operations in oil and gas fields. The cost of MFM in 2009 was estimated to be in the range of hundreds of thousands of dollars [4]. Hence, there is a large demand from the oil and gas industry for a reliable and inexpensive technique for MFM. The most popular available techniques for MFM can be categorized into seven classes based on their technology: conventional method or separation [5], impedance techniques [6]–[9], radio frequency (RF) sensor [10], resonant cavity sensors [11], [12], gamma-ray [13], x-ray [14], and Coriolis-microwave flow meter [15].

Manuscript received January 20, 2020; revised February 14, 2020; accepted February 18, 2020. Date of publication March 3, 2020; date of current version April 16, 2020. This work was supported by the Natural Sciences and Engineering Research Council of Canada under CRD Grants and Discovery Grants. (Corresponding author: *Fatemeh Modares Sabzevari*.)

Fatemeh Modares Sabzevari, Robert S. C. Winter, and Karumudi Rambabu are with the Electrical and Computer Engineering Department, University of Alberta, Edmonton, AB T6G 2V4, Canada (e-mail: modares@ualberta.ca; rswinter@ualberta.ca; rambabu@ualberta.ca).

Daniel Oloumi is with the Infineon Technologies Austria, 9500 Villach, Austria, and also was with the Electrical and Computer Engineering Department, University of Alberta, Edmonton, AB T6G 2V4, Canada (e-mail: daniel.oloumi@infineon.com).

Digital Object Identifier 10.1109/JSTARS.2020.2977303

However, none of the aforementioned techniques are appealing enough to be widely used in the industry. The conventional method is invasive and expensive [5]. Impedance techniques, which include electrical capacitance tomography (ECT), electrical resistance tomography (ERT), and magnetic induction tomography, need to identify the flow pattern before measurements. The low image quality makes it more complicated to distinguish different phases [16]. The accuracy of the RF sensor technique is dependent on the water percentage, and a lookup table is required [10]. The resonant cavity method cannot be used in situations with continually flowing fluids [11]. Gamma-ray and x-ray methods are costly to implement and not very popular due to safety aspects [10], [13], [14]. The combined microwave and Coriolis technique is bulky and hard to install [15].

Microwave sensing and imaging (MSI) is a noninvasive method for investigating internal structural properties [17]. Ultrawideband (UWB) synthetic aperture radar (SAR) technology can provide a high-resolution 2-D image in the range and cross-range directions [18], [19]. UWB SAR technology can be implemented in either the time domain or the frequency domain. In frequency domain postprocessing, the image is reconstructed based on the frequency components of the received UWB pulses. On the other hand, time domain postprocessing is based on projecting time domain signals into the spatial domain. Since frequency-domain postprocessing is still more complex [20], the time-domain postprocessing is preferred and applied in this study.

In the last decade, UWB radars have attracted attentions to be used in different applications [21], such as steam-flow monitoring [22], ice-road monitoring [23], biomedical imaging [24], [25], navigation [26], localization, and tracking of targets [27].

In this article, a noninvasive MSI method based on UWB SAR imaging is presented for MFM in crude oil pipelines. UWB SAR imaging provides a high-resolution and low-cost solution for the imaging of different phases in a multiphase flow. Then, by applying an edge detection algorithm, the reconstructed image is used to find different phases. Finally, each phase flow rate is estimated. Moreover, to increase the accuracy of the flow rate estimation, a generalized impulsization technique and a novel weak scatterer enhancement technique are presented and validated through simulation and experimental results. Also, the sectional image reconstruction for stratified flows is proposed to improve the image accuracy and flow rate estimation.

This article is organized as follows. Section II is dedicated to the problem statement and Section III describes the system

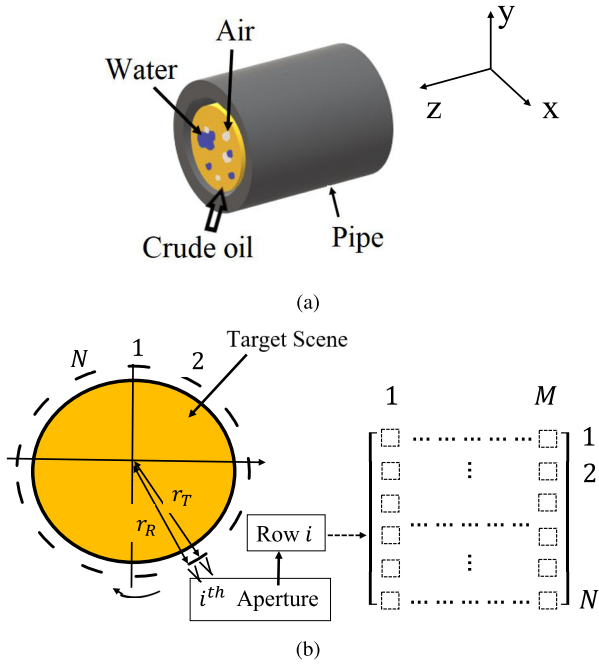


Fig. 1. (a) General crude oil pipe. (b) CSAR data acquisition.

configuration needed for the proposed technique. Section IV elaborates the simulations, and the experimental validation is presented in Section V. Finally, Section VI presents the conclusion.

## II. PROBLEM STATEMENT

In general, the flow in a crude oil pipe is a mixture of three main phases: water, oil, and gas [see Fig. 1(a)]. Petroleum operators need to monitor and measure the volume or flow rate of each phase before making decisions for possible further processing [4]. In some studies, different metrics such as fraction error [28] are used to evaluate MFM. The fraction error is defined as the deviation of each phase fraction from its true value. It should be noted that a specific fraction error in two pipes with different cross sections reflects different flow errors and might be confusing. Since the final goal of MFM is the flow metering of each phase, the flow rate error is considered as the metric in this study. The detailed explanation of the flow rate and flow rate error calculation is presented in the next section.

This article uses MSI technology to create a 2-D image of any arbitrary pipe cross section. The image is, then, used to estimate the area of each phase in a specific cross section,  $S(z)$ , where  $z$  is used to differentiate between the different cross sections. It is assumed that for a small-enough  $\Delta z$ :  $S(z_1) \simeq S(z_1 + \Delta z)$ , which implies the cross-sectional area of each phase is constant over  $\Delta z$ . Hence, the total volume of each phase can be represented as

$$V = S(z)\Delta z. \quad (1)$$

Consequently, the flow rate  $Q$  of each phase can be calculated as

$$Q = \frac{V}{\Delta t} = \frac{S(z)\Delta z}{\Delta t} = S(z) \times \bar{v} \quad (2)$$

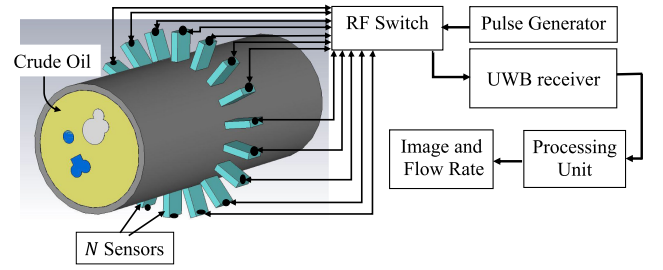


Fig. 2. System set-up.

where  $\bar{v}$  is the average velocity of the flow, which can be extracted using Doppler techniques [29]. Therefore, estimating  $S(z)$  leads to flow metering for each phase. Then, the flow rate error of each phase is calculated using the following formula:

$$\text{err} = \left| \frac{Q_{\text{cal}} - Q_{\text{true}}}{Q_{\text{true}}} \right| \times 100 \quad (3)$$

where  $Q_{\text{cal}}$  and  $Q_{\text{true}}$  are the estimated flow rate and the true flow rate, respectively.

It should be noted that the maximum average velocity of a multiphase flow in industrial oil–gas pipes is reported at 50 km/h or 13.8 m/s [30]. Since data acquisition of the proposed method is completed in 10 ms, the target scene can be modeled as a stationary problem in each cross section of the pipe.

## III. SYSTEM CONFIGURATION

A complete experimental set-up of MSI system for MFM is illustrated in Fig. 2. It consists of  $N$  sensors arranged in a circular fashion around the pipe. Each sensor includes two antennas: one is for transmitting and the other for receiving the reflected pulse from the multiphase fluid. The pulse generator generates a UWB pulse, and it connects to an RF switch box, which connects to the transmitter and receiver of the active sensor. In other words,  $N - 1$  sensors are inactive, and only one sensor is active at a time. The received signals from the sensors are processed to reconstruct the image and estimate the flow rate. The following section provides more details about circular SAR (CSAR) microwave imaging.

### A. Data Acquisition

A basic schematic of CSAR has been shown in Fig. 1(b), where  $N$  apertures are used for collecting data. At aperture position  $i$ , the transmitted and the backscattered signal can be written as

$$s_{T,i} = s(t) \quad (4)$$

$$s_{R,i} = A s'(t - \Delta t) \quad (5)$$

where  $A$ ,  $s'(t)$ , and  $\Delta t$  are the amplitude of the received signal, the time derivative of  $s(t)$ , and the round trip time of the pulse between the antenna and a scatterer, respectively [31]. Hence, the raw data will be in a matrix format with dimensions  $N \times M$ , where  $N$  and  $M$  are the number of apertures and the number of sampled points of the received pulse, respectively. In this article, the transmitted signal is a second derivative Gaussian

pulse, which can be written as [18]

$$s_{T,i} = \frac{2}{\tau^2} \exp\left(-\left(\frac{t}{\tau}\right)^2\right) \left(\frac{2t^2}{\tau^2} - 1\right) \quad (6)$$

where  $s_{T,i}$  and  $\tau$  are the second derivative Gaussian pulse and the time constant, respectively. The range resolution and the cross-range resolution of CSAR are the same and are estimated as [32]

$$\Delta_R = \frac{c}{3BW\sqrt{\varepsilon_r}} \quad (7)$$

where  $c$ ,  $BW$ , and  $\varepsilon_r$  are the speed of light in a vacuum, pulse bandwidth, and dielectric constant of the propagation medium, respectively. In order to remove the mutual coupling between the transmitter and the receiver, as well as ambient effects, a calibration process is needed. In this study, the calibrated signal is calculated as follows:

$$s_{c,i} = s_{\text{raw},i} - s_{\text{am},i}, \quad i = 1, 2, \dots, N \quad (8)$$

where  $s_{c,i}$ ,  $s_{\text{raw},i}$ , and  $s_{\text{am},i}$  are the calibrated signal, the raw signal, and the ambient signal in the presence of all other sensors for the aperture position  $i$ , respectively.

### B. Image Reconstruction

In this article, the time-domain global back-projection (TD-GBP) technique [33] has been applied to reconstruct 2-D images. The target scene is discretized into  $L$  and  $K$  grids in the  $x$  and  $y$  directions, respectively; hence, the output image is an  $L \times K$  matrix. For each  $l$  and  $k$ , the distance can be calculated as

$$\Delta R_{i,l,k} = \sqrt{(X_i - x_l)^2 + (Y_i - y_k)^2} \quad (9)$$

where  $(X_i, Y_i)$  and  $(x_l, y_k)$ , respectively, are the  $i$ th antenna aperture position and the corresponding position of the grid  $(l, k)$

$$\Delta t_i(l, k) = \frac{2\Delta R_{i,l,k}\sqrt{\varepsilon_r}}{c} \quad (10)$$

where  $\Delta t_i(l, k)$  is the time of flight between the grid  $(l, k)$  and the  $i$ th antenna position. It is considerably important that  $\varepsilon_r$ , which is the dielectric constant of the crude oil, is reported approximately constant in frequency span (1–7) GHz [34] and the crude oil can be considered as a nondispersive medium for the UWB propagation. Hence, it prevents happening Brillouin Precursors [35]

$$\text{image}(i, l, k) = s_{c,i} \left( \Delta t_i(l, k) \right) \quad (11)$$

$$\text{Image}(l, k) = \sum_{i=1}^N \text{image}(i, l, k) \quad (12)$$

where  $s_c$  is the calibrated data. It should be noted that the Image value depends on the pulse width and pulse side lobes. Different format of the image are proposed to evaluate different dielectric interfaces and sharpen the boundaries of the target in the image by eliminating the side lobe effects of the received pulse [36]. The real image, positive image, and absolute image were defined

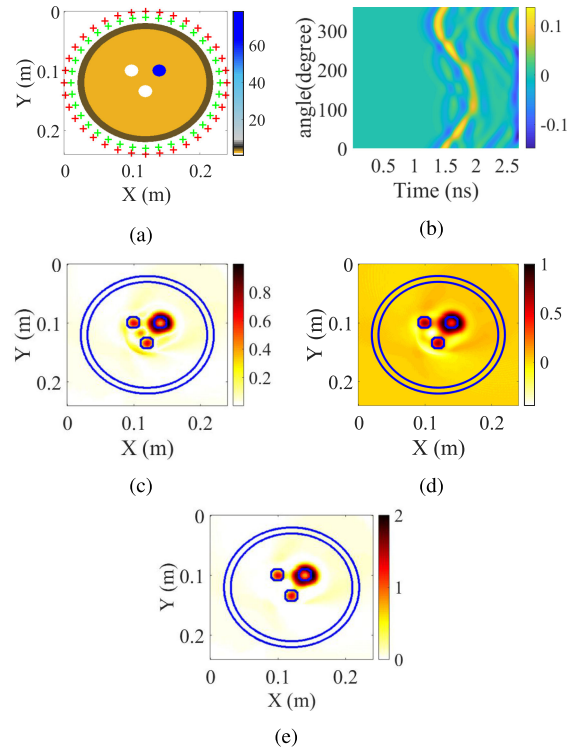


Fig. 3. (a) Simulation set-up. (b) Calibrated data. (c) Absolute image. (d) Real image. (e) Positive image.

in [32] and [36] as

$$\text{Real Image} = \text{real}\{\text{Image}\} \quad (13)$$

$$\text{Absolute Image} = \|\text{Image}\| \quad (14)$$

$$\text{Positive Image} = \text{real}\{\text{Image}\} + \|\text{Image}\|. \quad (15)$$

## IV. IMAGING AND FLOW METERING

Different flow patterns in oil pipes have been reported, including dispersed bubble flow, stratified, slug, and annular flow [37]. In this article, the first two types of flows are considered. The following sections describe the imaging techniques for both cases.

### A. Dispersed Bubble Flow

In this section, several dispersed bubble flow scenarios are investigated. A three-phase scenario, which includes a water bubble and two air bubbles in crude oil, as shown in Fig. 3(a), is simulated using a 2-D finite difference time domain (FDTD) solver. The dielectric constants of water, air, and crude oil are considered to be: 78, 1, and 2.1, respectively. Since the bubble size is in the range of 3–23 mm [38], all three bubbles are considered as circles with a radius of 10 mm. The most frequently used pipes are made of glass-reinforced plastic, also known as fiberglass composites; and the diameter is reported as 10.2 cm [39]. The dielectric constant of the fiberglass composites is in the range of 3.45–4.42 [40]. Therefore, the considered pipe has a dielectric constant of 4, and an inner radius of 9 cm with

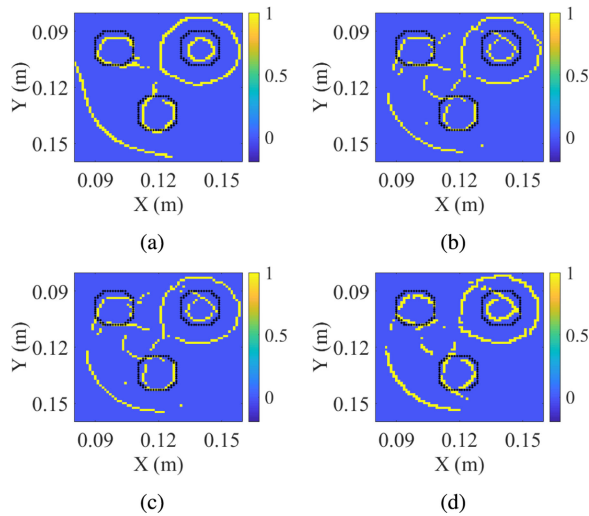


Fig. 4. (a) Canny edge detector. (b) Sobel edge detector. (c) Prewitt edge detector. (d) Roberts edge detector.

a thickness of 1 cm. In Fig. 3(a), the transmitters and receivers are shown as red and green “+” symbols. The transmitted signal is a second derivative Gaussian pulse with a full width at half maximum (FWHM) of 100 ps, which corresponds to a  $-10$  dB bandwidth of 4.12 GHz.

The calibrated data, the reconstructed real, positive, and absolute images are shown in Fig. 3. The reconstructed images clearly show air and water bubbles. However, the final goal of MFM is an automatic measurement of area or flow rate of each phase in the pipe. One possible solution is to detect edges in the reconstructed image, distinguish each phase boundary, and then, estimate the flow rate of each phase. The next section provides more details about edge detection algorithms.

1) *Edge Detection Algorithms for MFM*: Generally, edge detector algorithms apply a first- or second-order spatial derivative to the image and find the local maxima or zero-crossing points [41]. A wide range of edge detectors is presented and studied in [42]. Four of the most popular edge detectors are: Canny, Sobel, Prewitt, and Roberts. Canny edge detection is based on three objectives: 1) low error rate, 2) thin edges, and 3) accurate localization [43]. The Sobel edge detector performs a second derivative of the image luminance to extract the edges [44]. Prewitt and Roberts are two other gradient-edge detectors which use Prewitt and Roberts’ operators, respectively. For the case of MFM, the edge detection algorithm with the least error should be applied. To study the quality of edge detector algorithms, the four edge detectors are applied to the real image, shown in Fig. 3(d), and results are shown in Fig. 4. As can be seen, the Sobel and Prewitt detectors perform poorly and fail to successfully detect the continuous edge of the water target. The Robert operator output provides jagged edges. The evidence suggests that the Canny edge detector might be the best candidate for this application. The local maximum in spatial domain variation are considered as edges, and maximum variation of the pixels values in the real image and the positive image are equal; hence, the edge detection can be applied to either the real image or the positive image.

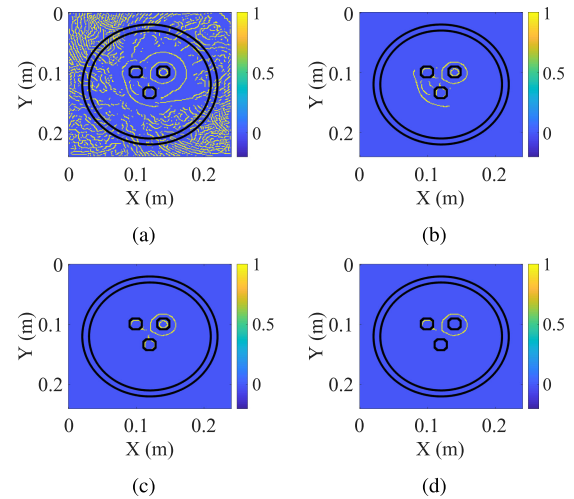


Fig. 5. Canny edge image. (a) Threshold = 0. (b) Threshold = 0.3. (c) Threshold = 0.6. (d) Threshold = 0.9.

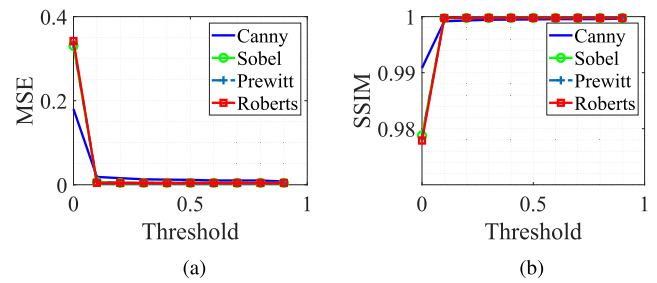


Fig. 6. (a) MSE versus threshold for all algorithms. (b) SSIM versus threshold for all algorithms.

The functionality of the edge detectors can be controlled by a threshold [45]. The edge detector threshold should be adjusted based on several factors such as the noise level and number of pixels [46]. The Canny edge detection is performed with four different thresholds, and the results are shown in Fig. 5. As can be seen, a zero threshold results in the detection of unnecessary edges. On the other hand, a 0.9 threshold fails to detect one of the target edges. While thresholds 0.3 and 0.6 are both successful at detecting all three targets edges, the 0.6 threshold is the best threshold for this case. A suitable threshold might be considered to be one in the range of 0.3–0.6. In a real-case scenario, the threshold adjustment requires prior information that can be attained by properly training the operators.

Although the flow rate error was previously defined by (3), some image criteria are needed to compare the extracted edges of the reconstructed image and the edges of the original image. The structural similarity (SSIM) Index, a popular criteria for measuring image qualities, was introduced in [47]. In this study, the SSIM and mean square error (MSE) are considered as criteria. To evaluate and compare the four algorithms, SSIM and MSE for different thresholds are estimated and the results are presented in Fig. 6(a) and (b), respectively. The MSE and SSIM values of Sobel, Prewitt, and Roberts are very close. The Canny algorithm performs better in low thresholds. It is important to



TABLE I  
PHASE ERROR

Phase	Error (%)
Air 1	16.1
Air 2	19.3
Water	43.9
Crude oil	2.1

note that neither a high SSIM nor a low MSE can be the only criteria for the quality of extracted edges. In other words, both image and MSE or SSIM are required to compare the quality of the extracted edges. For instance, a 0.3 threshold is not a successful edge detector, as shown in Fig. 5(b), since some extra lines are extracted as edges. However, this threshold results in a 0.998 SSIM, which shows high similarity of the detected and original edges. The flow rate error of each phase is calculated based on Fig. 5(d) and presented in Table I. Air bubbles and the water bubble generate more errors than the crude oil in flow rate estimation. The area of the water and air bubbles are small compared to that of the crude oil; therefore, a small deviation from the true value of the area causes a large error compared to the crude oil.

2) *Impulsization*: The ideal pulse for MSI is a Dirac delta function since this would have infinite range resolution. The pulse generators used in this experiment generates pulses with FWHM in the range of 80–100 ps. The impulsization technique is a surrogate postprocessing method to generate a definite image with sharp edges. A mathematical representation of this method [48] can be formulated as

$$\delta(s_{c,i}(t)) = \begin{cases} s_{c,i}(t_{\text{peak}}) & \text{if } t = t_{\text{peak}} \\ & \& s_{c,i}(t_{\text{peak}}) > T \\ 0 & \text{otherwise} \end{cases} \quad (16)$$

where  $t_{\text{peak}}$  and  $T$  are the time at which the  $s_{c,i}$  has a peak and a threshold for picking max values, respectively. The  $t_{\text{peak}}$  can be easily determined by finding the peaks of  $s_{c,i}$ . The idea of impulsization can be generalized by the following formula:

$$\delta_g(s_{c,i}(t)) = \begin{cases} s_{c,i}(t) & \text{if } |t - t_{\text{peak}}| < \Delta T \\ & \& s_{c,i}(t_{\text{peak}}) > T \\ 0 & \text{otherwise} \end{cases} \quad (17)$$

where  $\delta_g$  and  $\Delta T$  are a generalized impulsized signal and the specified time window, respectively. The choice of  $\Delta T$  depends on the pulse width and the level of noise. As shown in Fig. 4, the edge detection algorithms find two different circles, which correspond to the side lobes of the received pulse. In order to enhance the accuracy of the edges, the generalized impulsization technique has been used. Fig. 7(a) shows a scenario with an arbitrary nonsmooth water bubble. Fig. 7(b) and (f) shows the calibrated data and the corresponding edge image, respectively. Equation (17) with a  $\Delta T = 29.7$  ps, which is 20 time steps, is applied to the calibrated data and the positive image is shown in Fig. 7(e). As  $\Delta T$  decreases, the generalized impulsization method will be equivalent to transmitting a Dirac delta signal, i.e.,  $s(t) = \delta(t)$ . However, this technique does not increase the spatial resolution and only results in a nonblurred image, which is a perfect input for the edge detection algorithm. Fig. 7(g)

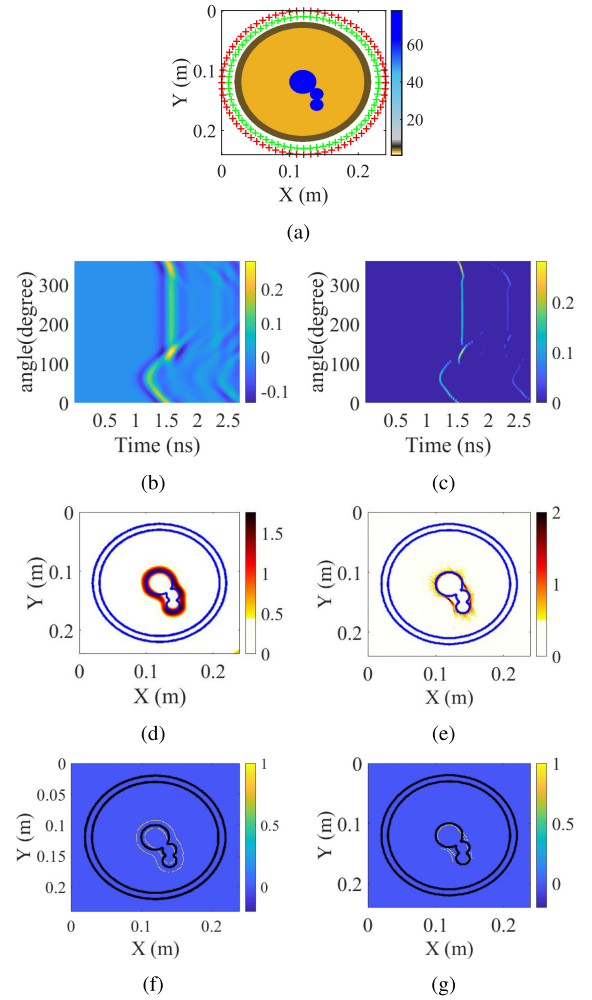


Fig. 7. (a) Simulation set-up. (b) Calibrated data. (c) Calibrated data applying generalized impulsization. (d) Positive image. (e) Positive image. (f) Edge image applying generalized impulsization. (g) Edge image applying generalized impulsization.

TABLE II  
PHASE ERROR

Phase	Error (%) (conventional technique)	Error (%) (impulsization technique)
Water	28.1	14.9
Oil	2.6	1.4

shows the edge image after applying generalized impulsization. The two inner and outer yellow lines in Fig. 7(f), caused by the pulse width, are merged in Fig. 7(g). There are some extra lines in Fig. 7(g). These lines are the drawback of the impulsization technique. The flow rate error of each phase is calculated and presented in Table II. The water flow rate error and oil flow rate error is improved to 14.9% and 1.4%, respectively.

3) *Weak Scatterer Enhancement*: MSI technology is based on the discontinuities in the permittivity of the materials. The magnitude of the received signal is proportional to the contrast of the target compared to the background. Hence, the reflected signal from the high contrast targets carries far more energy than the corresponding signal from the low contrast ones. To illustrate

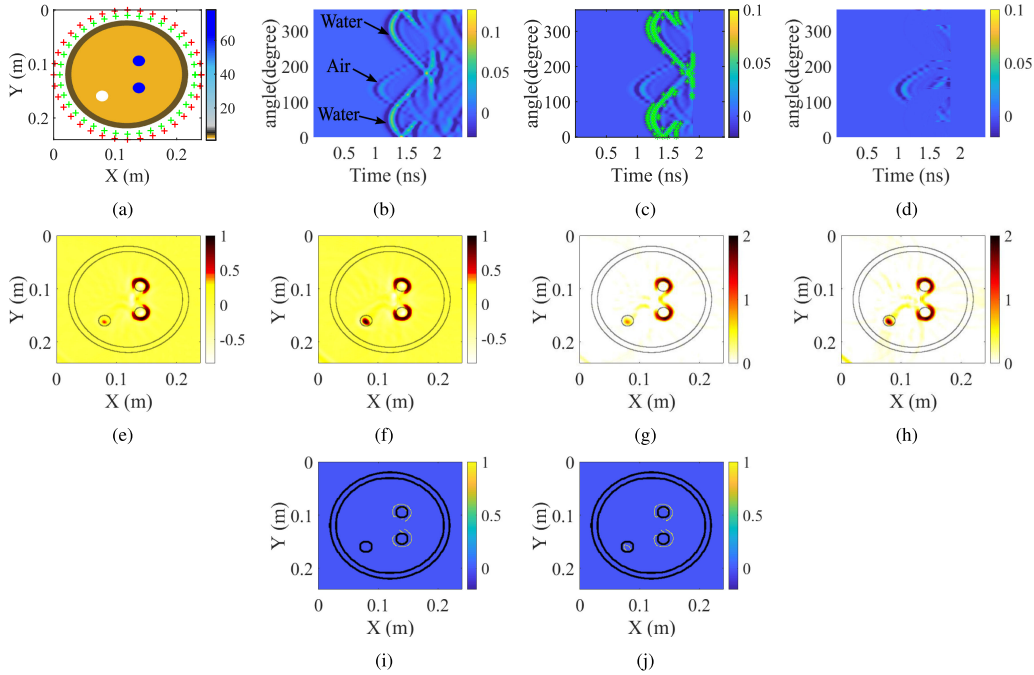


Fig. 8. (a) Simulation set-up. (b) Calibrated data. (c) Peaks with value greater than the threshold. (d) Modified calibrated data. (e) Conventional real image. (f) Real image applying weak scatterer enhancement. (g) Conventional positive image. (h) Positive image applying weak scatterer enhancement. (i) Conventional edge image. (j) Edge image applying weak scatterer enhancement.

this phenomenon, a three-phase scenario, as shown in Fig. 8(a), is simulated in the FDTD solver. In Fig. 8(b), the magnitude of the air sinogram is approximately three times weaker than that of the water sinogram. This causes a pale appearance in the reconstructed image, as shown in Fig. 8(e) and (g). When MSI is used in practical applications, the reconstructed image will be drastically affected due to the presence of noise and clutter [49]. A flowchart of the proposed novel weak scatterer sinogram enhancement algorithm is shown in Fig. 9. The algorithm takes  $s_c$  and  $W$ , the calibrated signal and the pulse width, as inputs. The peaks of the calibrated signal for the aperture position  $i$  are found, and their corresponding pulse segment is set to zero if  $s_{c,i}(t_{\text{peak}})$  is greater than a threshold ( $H_p$ ). This process repeats for all aperture positions, and the modified calibrated signal is, then, forwarded to the image reconstruction process. The steps of implementing the technique are presented in Algorithm 1.

Consider Fig. 10 for understanding steps 5–7. The blue curve is the  $s_{c,i}$ , i.e.,  $i = 10$ . The red line is the threshold line, and the detected peaks are marked with a circle. The green peaks are greater than the threshold. Step (5) removes the full pulse that correspond to the green labeled peaks. Finally, the  $s_{cm,i}$  is shown with a black line. It should be noted that the threshold is constant for all the aperture positions. One possible choice of threshold is to scale it with respect to the maximum value of  $|s_c|$ . Typically,  $H_p$  should be small enough to completely eliminate the strong reflection. On the other hand,  $H_p$  should be high enough to preserve the weak reflection. The best choice of  $H_p$  for the crude oil pipes is in the range of  $H_p = [0.3 \times \max\{|s_c|\} - 0.45 \times \max\{|s_c|\}]$ . The reconstructed image using  $s_{cm}$  only consists of weak scatterer targets. In order to present a complete image, which includes all of the targets, the image of the modified calibrated data is added to the original image.

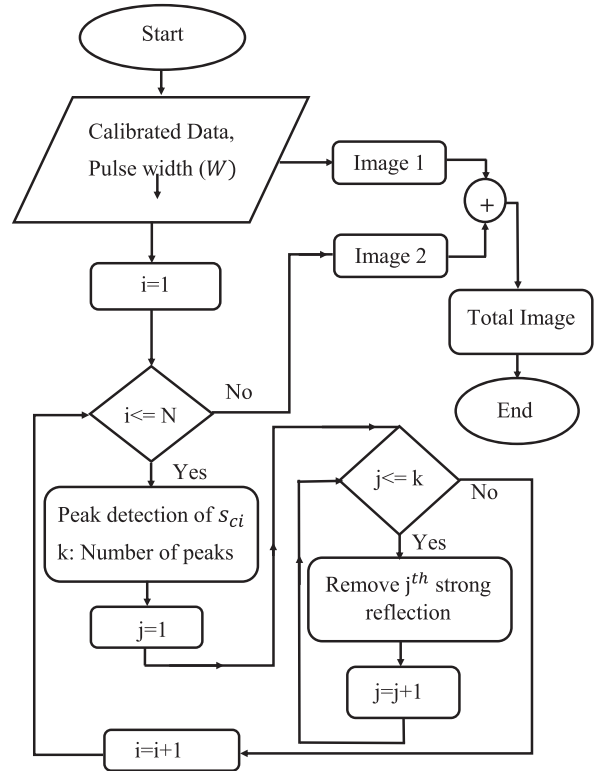


Fig. 9. Weak scatterer enhancement flowchart.

This novel method is applied to the time-gated calibrated data, which is shown in Fig. 8(b). The threshold has been chosen:  $H_p = 0.31 \times \max\{|s_c|\}$ . The green marked labels on Fig. 8(c) show the peaks that are greater than  $H_p$ . It is evident that the

**Algorithm 1:** Proposed Weak Scatterer Enhancement.

```

1: procedure WSE( $s_c, W$ )
2:    $s_c, W$ : inputs, Total Image: output
3:    $Image1 \leftarrow s_c$ 
4:   for  $i = 1, \dots, N$  do
5:     find the peaks of the  $s_{c,i}$ 
6:     for  $j = 1, \dots, k$  do
7:       if  $s_{c,i}(t_{peak}) > H_p$  then:
8:          $Image2 \leftarrow s_{cm}$ 
9:          $Total Image = Image1 + Image2$ 

```

$\triangleright W$ : Pulse width  
 $\triangleright$  Image reconstruction using TD-GBP  
 $\triangleright k$ : Number of peaks  
 $\triangleright H_p$ : Threshold  
 $\triangleright s_{cm,i}$ : modified calibrated signal  
 $\triangleright$  Image reconstruction using TD-GBP

$$s_{cm,i}(t) = \begin{cases} 0 & \text{if } |t - t_{peak}| < W/2 \\ s_{c,i}(t) & \text{otherwise,} \end{cases} \quad (18)$$

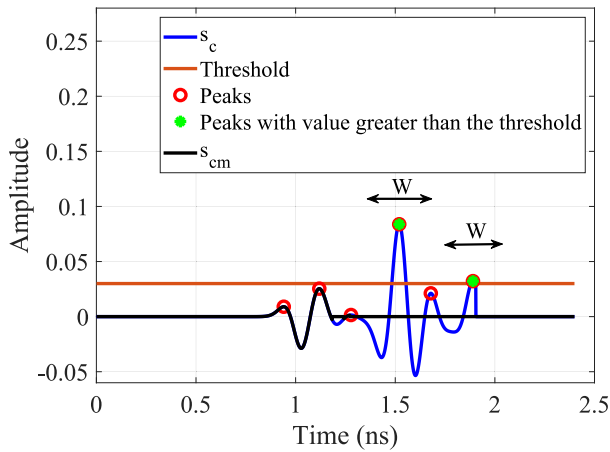


Fig. 10. Illustration of the weak scatterer enhancement.

TABLE III  
PHASE ERROR

Phase	Error (%) (conventional technique)	Error (%) (weak scatterer enhancement technique)
Water1	15.9	15.3
Water2	19.1	13.6
Air	100.0	60.0
Oil	0.9	0.4

algorithm removes the reflections corresponding to the water bubbles. The signature of water bubbles are mostly vanished in the calibrated data, but the air bubbles signature is left, as illustrated in Fig. 8(d). Conventional real and positive are shown in Fig. 8(e) and (g), respectively. The canny edge detector is applied to the positive image and the edge image is illustrated in Fig. 8(i). The air bubble appears as a pale target, and it has not been found by the edge detector. In Fig. 8(f), the air bubble is roughly as clear as water bubbles. The Canny edge detector is applied to the enhanced positive image and the air bubble is appeared in the edge image, as shown in Fig. 8(j). The flow rate errors for all targets and crude oil is calculated and presented in Table III. The flow rate error of the crude oil is improved to 0.4%.

**B. Stratified Flow**

In the stratified flow, different phases flow in a layered manner. Imaging of a stratified flow is barely addressed in the multiphase flow studies. For instance, in [50] and [51], two-phase stratified profiles are considered; however, the straight boundaries of the profiles are shown as curvy boundaries in the reconstructed images. MSI can provide a more accurate and reliable solution for MFM in a situation of stratified flow.

A numerical simulation setup is conducted, as shown in Fig. 11(a). In the layered structure, a uniform group velocity cannot be considered for the image reconstruction process. The sectional image reconstruction method, which is presented in [52], is applied to the stratified case. The principle behind the method consists of detecting different regions and, then, reconstructing the image using nonuniform group velocities. In a three-phase stratified flow, the first reflection from the bottom of the pipe is caused by the interface between the pipe and water. Similarly, the first reflection from the top of the pipe is caused by the interface between the pipe and air. The second and third reflections are caused by the air–oil and the oil–water interfaces, respectively. These three reflections appeared as peaks in the calibrated data and can be clearly seen in spatial-time data, as shown in Fig. 11(b). Hence, by finding peaks of  $s_{c,i}$ , the first, second, and third boundaries are identified. Then, nonuniform group velocity based on the group velocity of the corresponding regions is used in the image reconstruction process, as shown in Fig. 11(c). The conventional real and positive images are shown in Fig. 11(d) and (f), respectively. The sectional real and positive images are shown in Fig. 11(e) and (g), respectively. As shown in Fig. 11(d) and (f), curved borders have appeared between layers. However, the borders in the sectional images are not curved anymore and provide a more accurate illustration of each phase. Table IV suggests that the sectional image reconstruction improves the water, air, and oil flow rate errors to 12.2%, 10.3%, and 3.4%, respectively.

**V. EXPERIMENTAL VALIDATION**

To evaluate the proposed method, several two-phase and three-phase scenarios are conducted. Fig. 12 illustrates the

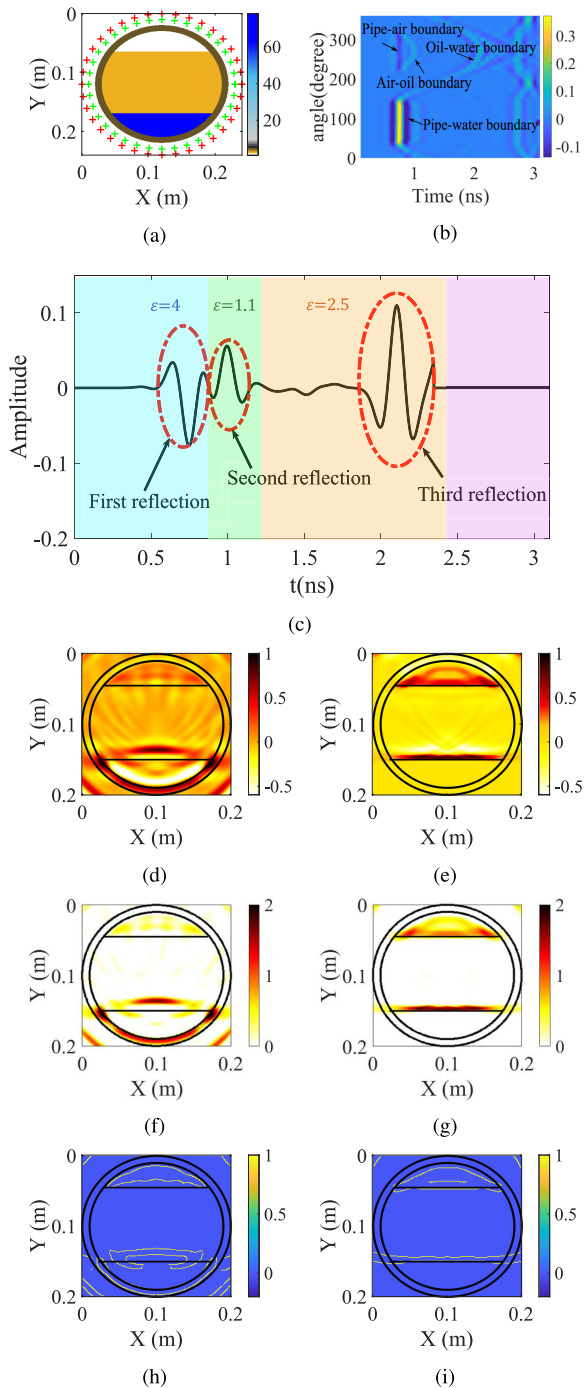


Fig. 11. Stratified flow case. (a) Simulation set-up. (b) Nonuniform group velocity in the sectional image reconstruction technique. (c) Calibrated data. (d) Conventional real image. (e) Real image applying sectional image reconstruction. (f) Conventional positive image. (g) Positive image applying sectional image reconstruction. (h) Conventional edge image. (i) Edge image applying sectional image reconstruction.

TABLE IV  
PHASE ERROR

Phase	Error (%) (conventional technique)	Error (%) (sectional technique)
Water	57.0	12.2
Air	41.0	10.3
Oil	4.6	3.4

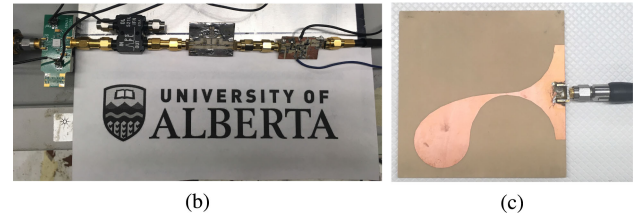
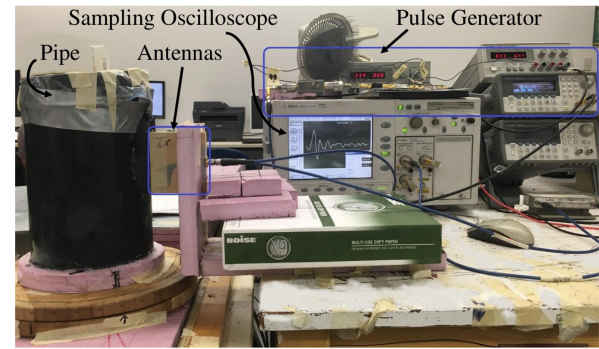


Fig. 12. (a) Measurement set-up. (b) Pulse Generator. (c) Vivaldi antenna.

TABLE V  
EXPERIMENT ONE-PHASE ERROR

Phase	Error (%) (conventional technique)	Error (%) (impulsization technique)
Water	65.9	15.0
Oil	1.3	0.3

experimental setup, pulse generator, and Vivaldi antennas, which are used as transmitter and receiver. The pulse generator feeds the sensors with a first derivative Gaussian pulse with an approximate FWHM of 82 ps, which corresponds to a  $-10$  dB bandwidth of 5.9 GHz at 1 MHz PRF. The received signal is measured by a sampling oscilloscope and, then, processed to reconstruct the image and estimate the flow rate. In all the experiments, a polyvinyl chloride pipe and diesel fuel are used to emulate the industrial set-up since their dielectric constants are 4 and 2.1, respectively [55], [56]. The inner radius of the pipe is 7.7 cm with a 0.8 cm thickness. The first experiment is a two-phase flow monitoring with a water bubble, which is emulated by placing a water-filled pipe with a radius of 1.1 cm in the diesel. The calibrated signal is calculated using (8), where  $s_{am}$  is the measured signal in the presence of the pipe containing the diesel. Hence, the reconstructed images would not include the pipe. As shown in Fig. 13(a), the positive image is blurry, and the edges are not fully matched to the dimension of the water bubble. After impulsization of the calibrated data, the improved positive image is shown in Fig. 13(b). Although the conventional positive image of the target is smoother, the improved positive image is more precise in terms of bubble dimension. As it is mentioned in Table V, the water and oil flow rate error improved to 15.0% and 0.3%, respectively.

In the second experiment, an additional pipe with an 11 mm radius filled with air is placed in the diesel. The distance between the two targets is 21 mm. The real and positive images are shown in Fig. 14. It should be noted that the dielectric constant of water



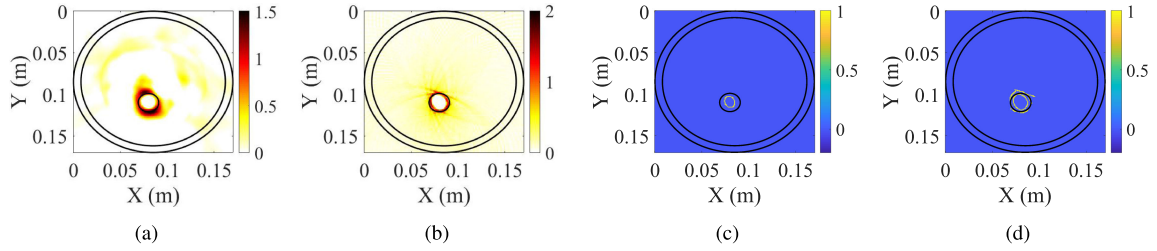


Fig. 13. Experiment 1: two-phase scenario. (a) Conventional positive image. (b) Positive image applying impulsization. (c) Conventional edge image. (d) Edge image applying generalized impulsization.

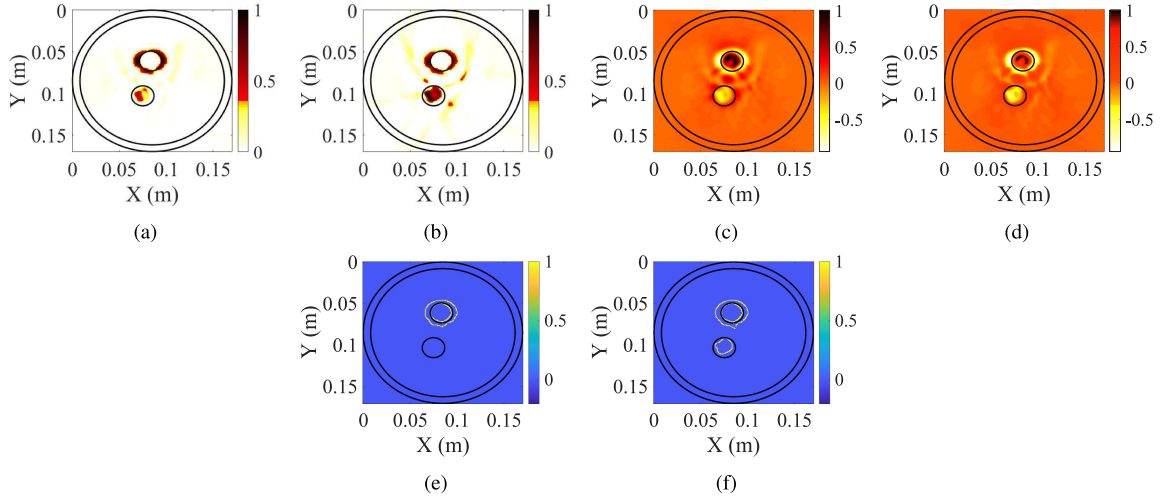


Fig. 14. Experiment 2: three-phase scenario. (a) Conventional positive image. (b) Positive image applying weak scatterer enhancement. (c) Conventional real image. (d) Real image applying weak scatterer enhancement. (e) Conventional edge image. (f) Edge image applying weak scatterer enhancement.

TABLE VI  
EXPERIMENT TWO-PHASE ERROR

Phase	Error (%) (conventional technique)	Error (%) (weak scatterer enhancement technique)
Water	10.0	10.8
Air	100.0	30.0
Oil	2.3	0.7

TABLE VII  
EXPERIMENT THREE-PHASE ERROR

Phase	Error (%)
Water	23.0
Air 1	18.0
Air 2	24.0
Oil	0.4

TABLE VIII  
EXPERIMENT FOUR-PHASE ERROR

Phase	Error (%)
Water	16.9
Air	7.0
Oil	3.8

is more than that of diesel, whereas the dielectric constant of air is less than that of diesel. Hence, the received signals from water and air have different polarity. Therefore, the water bubble has a positive value and the air bubble has a negative value in the reconstructed image. The Canny edge detector with a 0.6 threshold is applied to the real image and only the stronger scatterer, water bubble, is detected. The weak scatterer enhancement technique, as discussed in Section IV-A-3, is applied, and the results are shown in Fig. 14(b), (d), and (f). As it is mentioned in Table VI, the oil flow rate error improved to 0.7%.

The third experiment includes a water bubble and two air bubbles. The distances between the three targets are 15, 18, and 21 mm. The reconstructed real and absolute images are shown in Fig. 15. The Canny edge detector with a 0.3 threshold successfully identified three bubbles. The area and flow rate of each bubble is estimated and, then, flow rate errors are summarized in Table VII. It should be noted that for the first

three experiments,  $\varepsilon_r$  in the image reconstruction process is set to 2.1 based on the prior knowledge.

The last experiment investigates the stratified flow situation. The setup includes a water layer, a diesel layer, and an air layer, from bottom to top. The height of each phase is 37, 62.7, and 55.3 mm, respectively. The sectional real, positive, and edge images are shown in Fig. 16, and the error of each layer is summarized in Table VIII. Table IX summarizes the existing studies for MFM, a brief look of which may suggest that

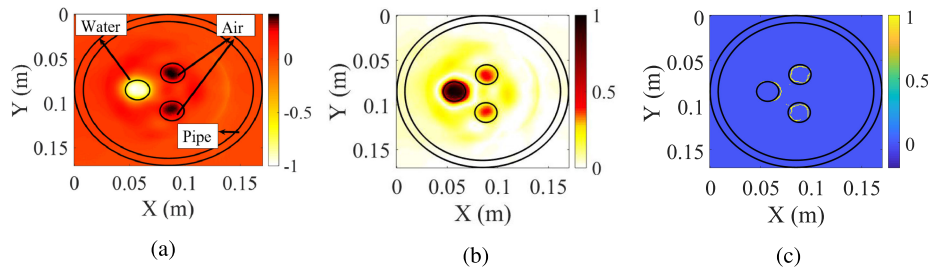


Fig. 15. Experiment 3: three-phase scenario. (a) Real image. (b) Positive image. (c) Edge image.

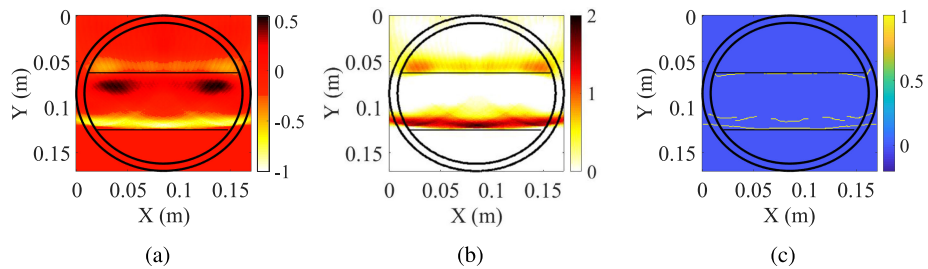


Fig. 16. Experiment 4: three-phase stratified scenario. (a) Sectional real image. (b) Sectional positive image. (c) Sectional edge image.

TABLE IX  
COMPARISON TABLE FOR THE EXISTING MULTIPHASE FLOW MEASUREMENT

Reference	Technology	Frequency	Complexity	Error Criteria	Error	Flow Monitoring	Cost	Limitations
[10]	RF Sensor	250 Hz	low	permittivity	30	No	low	non-metallic pipe
[28]	Gamma-ray	order $10^{19}$ Hz	high	root mean square error (RMSEP)	39	No	very high	safety aspects, limited to high water concentration
[8]	ECT/ERT Dual modality	200 kHz (for ECT)	high	-	-	Yes	high	oil continues flow needed for ECT, flow phase dependent
[53]	Resonant Cavity Sensor	100-350 Hz	high	-	-	No	high	only used for limited fraction of water, sensitive to water
[50]	CT and Cross-Entropy	order $10^{19}$ Hz	high	Relative Error (RE)	10	Yes	high	safety aspects, non-metallic pipe
[54]	X-Ray	order $10^{16}$ Hz	very high	-	-	No	very high	health risks, low accuracy
Proposed	UWB	2-10 GHz	low	Crude Flow Error	3.8	Yes	low	non-metallic pipe

UWB SAR technique might be a good candidate for industrial applications.

## VI. CONCLUSION

In this article, the UWB SAR technique is used for the purpose of multiphase monitoring and metering of crude oil pipelines. Several two-phase and three-phase dispersed bubble flows and a stratified flow are considered in the experiments. First, a two-phase scenario, a water bubble in a diesel pipe, is investigated, and the generalized pulse impulsization technique is applied to reduce the error in flow estimation. Second, a three-phase scenario, including one water bubble and one air bubble in the diesel, is considered, and a method for enhancing a weak scatterer image is applied to improve the air bubble imaging in the reconstructed images. Also, a more complicated scenario, including two air bubbles and one water bubble, is experimented. Finally, a three-phase stratified flow experiment is carried out, and the sectional image reconstruction technique

is used to enhance the image and the flow estimation of each phase. The estimated crude oil flow error is less than 4% in all the experiments, which shows that the proposed method can be applied in an industrial setting.

## ACKNOWLEDGMENT

The authors would like to thank Dr. R. Feghhi for helpful discussions.

## REFERENCES

- [1] E. N. dos Santos, R. L. de Paiva Rodrigues, D. R. Pipa, R. E. M. Morales, and M. J. da Silva, "Three-dimensional bubble shape estimation in two-phase gas-liquid slug flow," *IEEE Sensors J.*, vol. 18, no. 3, pp. 1122–1130, Feb. 2018.
- [2] Q. Su, C. Tan, and F. Dong, "Measurement of oil–water two-phase flow phase fraction with ultrasound attenuation," *IEEE Sensors J.*, vol. 18, no. 3, pp. 1150–1159, Feb. 2018.
- [3] F. R. M. da Mota, D. J. Pagano, and M. E. Stasiak, "Water volume fraction estimation in two-phase flow based on electrical capacitance tomometry," *IEEE Sensors J.*, vol. 18, no. 16, pp. 6822–6835, Aug. 2018.

- [4] G. Falcone, G. Hewitt, and C. Alimonti, *Multiphase Flow Metering: Principles and Applications* Developments in Petroleum Science. New York, NY, USA: Elsevier Science, 2009.
- [5] Z. Wu, "Developing a microwave tomographic system for multiphase flow imaging: Advances and challenges," *Trans. Inst. Meas. Control*, vol. 37, no. 6, pp. 760–768, 2015.
- [6] F. R. M. da Mota, D. J. Pagano, and M. E. Stasiak, "Water volume fraction estimation in two-phase flow based on electrical capacitance tomometry," *IEEE Sensors J.*, vol. 18, no. 18, pp. 6822–6835, Aug. 2018.
- [7] C. N. Strizzolo and J. Converti, "Capacitance sensors for measurement of phase volume fraction in two-phase pipelines," *IEEE Trans. Instrum. Meas.*, vol. 42, no. 3, pp. 726–729, Jun. 1993.
- [8] Yi Li and W. Yang, "Measurement of multi-phase distribution using an integrated dual-modality sensor," in *Proc. IEEE Int. Workshop Imag. Syst. Technol.*, May 2009, pp. 335–339.
- [9] E. Dyksteen, A. Hallanger, E. Hammer, E. Samnøy, and R. Thorn, "Non-intrusive three-component ratio measurement using an impedance sensor," *J. Phys. E, Sci. Instrum.*, vol. 18, pp. 540–544, Jun. 1985.
- [10] M. Tayyab, M. S. Sharawi, and A. Al-Sarkhi, "A radio frequency sensor array for dielectric constant estimation of multiphase oil flow in pipelines," *IEEE Sensors J.*, vol. 17, no. 18, pp. 5900–5907, Sep. 2017.
- [11] H. E. de Lima Ávila, D. J. Pagano, and F. R. de Sousa, "Water fraction measurement using a RF resonant cavity sensor," in *Proc. 19th Symp. IMEKO TC Symp., 17th IWADC Workshop Adv. Instrum. Sensors Interoperability*, 2013, pp. 281–285.
- [12] H. E. de Lima Ávila, D. J. Pagano, and F. R. de Sousa, "Improving the performance of an RF resonant cavity water-cut meter using an impedance matching network," *Flow Meas. Instrum.*, vol. 43, pp. 14–22, 2015.
- [13] B. K. Arvoh, R. Hoffmann, and M. Halstensen, "Estimation of volume fractions and flow regime identification in multiphase flow based on gamma measurements and multivariate calibration," *Flow Meas. Instrum.*, vol. 23, no. 1, pp. 56–65, 2012.
- [14] V. R. Bom *et al.*, "Accuracy aspects in multiphase flow metering using x-ray transmission," *IEEE Trans. Nucl. Sci.*, vol. 48, no. 6, pp. 2335–2339, Dec. 2001.
- [15] P. Mehdizadeh *et al.*, "Multiphase meter production well testing applied to low-GOR mature fields," in *Proc. SPE Prod. Oper. Symp.*, Apr. 2009.
- [16] I. M. Saied, M. Meribout, E. Kato, and X. H. Zhao, "Terahertz spectroscopy for measuring multiphase fractions," *IEEE Trans. THz Sci. Technol.*, vol. 7, no. 3, pp. 250–259, May 2017.
- [17] J. Laviada, M. T. Ghasr, M. López-Portugués, F. Las-Heras, and R. Zoughi, "Real-time multiview SAR imaging using a portable microwave camera with arbitrary movement," *IEEE Trans. Antennas Propag.*, vol. 66, no. 12, pp. 7305–7314, Dec. 2018.
- [18] D. Oloumi, J. Ting, and K. Rambabu, "Design of pulse characteristics for near-field UWB-SAR imaging," *IEEE Trans. Microw. Theory Technol.*, vol. 64, no. 8, pp. 2684–2693, Aug. 2016.
- [19] R. S. C. Winter, D. Oloumi, and K. Rambabu, "Virtually developed synthetic aperture radar: Theory, simulation, and measurements," *IEEE Trans. Geosci. Remote Sens.*, vol. 57, no. 5, pp. 2855–2863, May 2019.
- [20] Y. Wang and A. E. Fathy, "Advanced system level simulation platform for three-dimensional UWB through-wall imaging SAR using time-domain approach," *IEEE Trans. Geosci. Remote Sens.*, vol. 50, no. 5, pp. 1986–2000, May 2012.
- [21] D. Oloumi, P. Boulanger, A. Kordzadeh, and K. Rambabu, "Breast tumor detection using UWB circular-SAR tomographic microwave imaging," in *Proc. 37th Annu. Int. Conf. IEEE Eng. Med. Biol. Soc.*, Aug. 2015, pp. 7063–7066.
- [22] D. Oloumi, K. K. Chan, P. Boulanger, and K. Rambabu, "SADG process monitoring in heavy oil reservoir using UWB radar techniques," *IEEE Trans. Microw. Theory Technol.*, vol. 64, no. 6, pp. 1884–1895, Jun. 2016.
- [23] S. Gogineni, J. B. Yan, D. Gomez, F. Rodriguez-Morales, J. Paden, and C. Leuschen, "Ultra-wideband radars for remote sensing of snow and ice," in *Proc. IEEE MTT-S Int. Microw. RF Conf.*, Dec. 2013, pp. 1–4.
- [24] T. M. Grzegorzczak, P. M. Meaney, P. A. Kaufman, R. M. diFlorio-Alexander, and K. D. Paulsen, "Fast 3-d tomographic microwave imaging for breast cancer detection," *IEEE Trans. Med. Imag.*, vol. 31, no. 8, pp. 1584–1592, Aug. 2012.
- [25] D. Oloumi, K. Rambabu, and P. Boulanger, "Tracking a biopsy needle inside a breast using UWB circular-SAR," in *Proc. IEEE Int. Symp. Antennas Propag. USNC/URSI Nat. Radio Sci. Meeting*, Jul. 2015, pp. 534–535.
- [26] J. C. Adams, W. Gregorovich, L. Capots, and D. Liccardo, "Ultra-wideband for navigation and communications," in *Proc. IEEE Aeros. Conf. Proc.*, Mar. 2001, vol. 2, pp. 2/785–2/792.
- [27] D. Kocur, J. Fortes, and M. Švecová, "Multiple moving person tracking by UWB sensors: The effect of mutual shielding persons and methods reducing its impacts," *EURASIP J. Wireless Commun. Netw.*, vol. 2017, Apr. 2017, Art. no. 68.
- [28] B. K. Arvoh, R. Hoffmann, and M. Halstensen, "Estimation of volume fractions and flow regime identification in multiphase flow based on gamma measurements and multivariate calibration," *Flow Meas. Instrum.*, vol. 23, no. 1, pp. 56–65, 2012.
- [29] D. Kouame, J. Girault, J. Remenieras, J. Chemla, and M. Lethiecq, "High resolution processing techniques for ultrasound doppler velocimetry in the presence of colored noise. ii. multiplephase pipe-flow velocity measurement," *IEEE Trans. Ultrason. Ferroelectr. Freq. Control*, vol. 50, no. 3, pp. 267–278, Mar. 2003.
- [30] "Engineering ToolBox," 2001. [Online]. Available: [https://www.engineeringtoolbox.com/flow-velocity-steam-pipes-d\\_387.html](https://www.engineeringtoolbox.com/flow-velocity-steam-pipes-d_387.html), Accessed on: May 31, 2019.
- [31] L. Li, A. E. Tan, K. Jhamb, and K. Rambabu, "Characteristics of ultra-wideband pulse scattered from metal planar objects," *IEEE Trans. Antennas Propag.*, vol. 61, no. 6, pp. 3197–3206, Jun. 2013.
- [32] D. Oloumi, "Ultra-wideband synthetic aperture radar imaging: Theory and applications," Ph.D. dissertation, Univ. Alberta, Edmonton, AB, Canada, 2016.
- [33] P. R. Foster, J. D. Halsey, and M. G. M. Hussain, "Introduction to ultra-wideband radar systems," in *Proc. Ultra-Wideband Antenna Tech.*, Ch. 5, 1995.
- [34] K. Folgerø, A. Tomren, and S. Frøyen, "Permittivity calculator method and tool for calculating the permittivity of oils from PVT data," in *Proc. 30th Int. North Sea Flow Meas. Workshop*, Oct. 2012.
- [35] M. Dawood and K. Li, "Detection of brillouin precursors at microwave frequencies through a rectangular waveguide filled with wet soil," *IEEE Geosci. Remote Sens. Lett.*, vol. 15, no. 7, pp. 1065–1069, Jul. 2018.
- [36] D. Oloumi, M. I. Pettersson, P. Mousavi, and K. Rambabu, "Imaging of oil-well perforations using UWB synthetic aperture radar," *IEEE Trans. Geosci. Remote Sens.*, vol. 53, no. 8, pp. 4510–4520, Aug. 2015.
- [37] H. Ahmed, "Capacitance sensors for void-fraction measurements and flow-pattern identification in air-oil two-phase flow," *IEEE Sensors J.*, vol. 6, no. 5, pp. 1153–1163, Oct. 2006.
- [38] S. A. Sulaiman and N. A. Z. Kamarudin, "Bubbles size estimation in liquid flow through a vertical pipe," *J. Appl. Sci.*, vol. 12, pp. 2464–2468, 2012.
- [39] P. Trifunović, "Use of composite materials in oil industry," *Podzemni Radovi*, no. 19, pp. 157–164, Dec. 2011.
- [40] V. Sokolov, S. Shalgunov, I. Gurtovnik, L. Mikheeva, and I. Simonov-Emel'yanov, "Dielectric characteristics of glass fibre reinforced plastics and their components," *Int. Polym. Sci. Tech.*, vol. 32, no. 7, pp. 62–67, 2005.
- [41] P. Bao, L. Zhang, and X. Wu, "Canny edge detection enhancement by scale multiplication," *IEEE Trans. Pattern Anal. Mach. Intell.*, vol. 27, no. 9, pp. 1485–1490, Sep. 2005.
- [42] Y. Zheng, J. Rao, and L. Wu, "Edge detection methods in digital image processing," in *Proc. 5th Int. Conf. Comput. Sci. Educ.*, Aug. 2010, pp. 471–473.
- [43] M. Baştan, S. S. Bukhari, and T. Breuel, "Active canny: Edge detection and recovery with open active contour models," *IET Image Process.*, vol. 11, no. 12, pp. 1325–1332, 2017.
- [44] S. Jin, W. Kim, and J. Jeong, "Fine directional de-interlacing algorithm using modified sobel operation," *IEEE Trans. Consumer Electron.*, vol. 54, no. 2, pp. 587–862, May 2008.
- [45] G. N. Chaple, R. D. Daruwala, and M. S. Gofane, "Comparisons of Robert, Prewitt, Sobel operator based edge detection methods for real time uses on FPGA," in *Proc. Int. Conf. Technologies Sustain. Develop.*, Feb. 2015, pp. 1–4.
- [46] M. B. Ahmad and T.-S. Choi, "Local threshold and boolean function based edge detection," *IEEE Trans. Consum. Electron.*, vol. 45, no. 3, pp. 674–679, Aug. 1999.
- [47] Z. Wang, A. C. Bovik, H. R. Sheikh, and E. P. Simoncelli, "Image quality assessment: From error visibility to structural similarity," *IEEE Trans. Image Process.*, vol. 13, no. 3, pp. 600–612, Apr. 2004.
- [48] J. Ting, D. Oloumi, and K. Rambabu, "FMCW sar system for near-distance imaging applications—Practical considerations and calibrations," *IEEE Trans. Microw. Theory Technol.*, vol. 66, no. 1, pp. 450–461, Jan. 2018.
- [49] Q. Dou, L. Wei, D. R. Magee, and A. G. Cohn, "Real-time hyperbola recognition and fitting in GPR data," *IEEE Trans. Geosci. Remote Sens.*, vol. 55, no. 1, pp. 51–62, Jan. 2017.

- [50] Q. Wang, H. Wang, K. Hao, and P. Dai, "Two-phase flow regime identification based on cross-entropy and information extension methods for computerized tomography," *IEEE Trans. Instrum. Meas.*, vol. 60, no. 2, pp. 488–495, Feb. 2011.
- [51] M. H. Fazalul Rahiman, R. Abdul Rahim, M. H. Fazalul Rahiman, and M. Tajjudin, "Ultrasonic transmission-mode tomography imaging for liquid/gas two-phase flow," *IEEE Sensors J.*, vol. 6, no. 6, pp. 1706–1715, Dec. 2006.
- [52] D. Oloumi, R. S. C. Winter, A. Kordzadeh, P. Boulanger, and K. Rambabu, "Microwave imaging of breast tumor using time-domain UWB circular-SAR technique," *IEEE Trans. Med. Imag.*, to be published, doi: [10.1109/TMI.2019.2937762](https://doi.org/10.1109/TMI.2019.2937762).
- [53] S. R. Wylie, A. Shaw, and A. I. Al-Shammaa, "RF sensor for multiphase flow measurement through an oil pipeline," *Meas. Sci. Technol.*, vol. 17, pp. 2141–2149, Jul. 2006.
- [54] V. R. Bom *et al.*, "Accuracy aspects in multiphase flow metering using x-ray transmission," *IEEE Trans. Nucl. Sci.*, vol. 48, no. 6, pp. 2335–2339, Dec. 2001.
- [55] E. R. Fitzgerald and R. F. Miller, "Dielectric properties of the system polyvinyl chloride-dimethylthianthrene," *J. Colloid Sci.*, vol. 8, no. 1, pp. 148–169, 1953.
- [56] N. Ahmadian, S. Hasan, and O. P. N. Calla, "Permittivity and backscattering coefficient of diesel oil-contaminated soil at c band (5.3 ghz)," *Int. J. Microw. Sci. Technol.*, vol. 2013, 2013, Art. no. 950862.



**Fatemeh Modares Sabzevari** (Student Member, IEEE) received the B.Sc. and M.Sc. degrees in electrical engineering from the Iran University of Science and Technology, Tehran, Iran, in 2013 and 2016, respectively. She is currently working toward the Ph.D. degree in electrical and computer engineering with the University of Alberta, Edmonton, AB, Canada.

Her current research interests include microwave sensing and imaging for industrial applications, material characterization techniques, signal processing, and machine learning.



**Robert S. C. Winter** (Student Member, IEEE) received the B.Sc. degree in engineering physics in 2016 from the University of Alberta, Edmonton, AB, Canada, where he is currently working toward the Ph.D. degree in electrical and computer engineering.

His current research interests include radar and microwave sensing and imaging for biomedical and industrial applications as well as signal processing and machine learning.

Dr. Winter received the Alberta Graduate Excellence Scholarship, Queen Elizabeth II Graduate Scholarship, and the NSERC Undergraduate Student Research Award.



**Daniel Oloumi** (Member, IEEE) received the M.Sc. degree from the Blekinge Institute of Technology, Karlskrona, Sweden, in 2012, and Ph.D. degree from the University of Alberta, Edmonton, AB, Canada, in 2016, both in electrical engineering.

He was a Postdoctoral Fellow with the University of Calgary, April 2017 to January 2019, where he developed a low cost and portable ultrawideband (UWB) pulse radar. He is currently working at Infineon Technologies Austria AG, Villach, Austria.

Since 2007, he has been involved in the design, fabrication, and measurement of a variety of RF components, antennas, and radar systems. His current research interests include developing UWB radar systems, radar imaging, and signal processing techniques for industrial and biomedical applications as well as high power amplifiers using GaN technology.

Dr. Oloumi received the prominent T. Chen Fong, honorary Killam, and NSERC Postdoctoral Fellowships with The University of Calgary. He received the Andrew Steward Memorial graduate prize, the Izaak Walton Killam Award, the AITF and NSERC IPS2 scholarships at the University of Alberta, and also the MTT Graduate Fellowship for his work on oil well monitoring using UWB radar technology during his Ph.D. studies. His M.Sc. thesis was selected as the best thesis and awarded by Sparbanksstiftelsen Kronan.



**Karumudi Rambabu** (Member, IEEE) received the Ph.D. degree in electrical and computer engineering from the University of Victoria, Victoria, BC, Canada, in 2005.

He was a Research Member with the Institute for Infocomm Research, Singapore, from 2005 to 2007. Since 2007, he has been an Assistant Professor with the Department of Electrical and Computer Engineering, University of Alberta, Edmonton, AB, Canada, where he is currently a Professor. He is currently involved in oil well monitoring, pipeline inspection,

through wall imaging, vital sign monitoring, and biopsy needle guiding using ultrawideband (UWB) radar systems. His current research interests include design and development of UWB technology, and components and systems for various applications.

Dr. Rambabu received the Andy Farquharson Award for excellence in graduate student teaching from the University of Victoria in 2003 and the Governor Generals Gold Medal for the Ph.D. research in 2005. He serves as an Associate Editor for the *IET Microwaves, Antennas and Propagation*.